JOURNAL OF SYNCHROTRON RADIATION

ISSN 1600-5775

Received 18 September 2018
Accepted 7 January 2019

Edited by S. M. Heald, Argonne National Laboratory, USA

Keywords: dirhodium(II) tetraacetate; thiol; thiolate; structure; EXAFS; UV–vis; TD-DFT.

Supporting information: this article has supporting information at journals.iucr.org/s

Reactions of $Rh_2(CH_3COO)_4$ with thiols and thiolates: a structural study

Alejandra Enriquez Garcia, Farideh Jalilehvand* and Pantea Niksirat

Department of Chemistry, University of Calgary, 2500 University Drive NW, Calgary, Alberta, Canada T2N 1N4. *Correspondence e-mail: faridehj@ucalgary.ca

The structural differences between the aerobic reaction products of $Rh_2(AcO)_4$ (**1**; $AcO^- = CH_3COO^-$) with thiols and thiolates in non-aqueous media are probed by X-ray absorption spectroscopy. For this study, ethanethiol, dihydrolipoic acid (DHLA; a dithiol) and their sodium thiolate salts were used. Coordination of simple thiols to the axial positions of $Rh_2(AcO)_4$ with Rh—SH bonds of 2.5–2.6 Å keeps the Rh^{II}—Rh^{II} bond intact (2.41 ± 0.02 Å) but leads to a colour change from emerald green to burgundy. Time-dependent density functional theory (TD-DFT) calculations were performed to explain the observed shifts in the electronic (UV–vis) absorption spectra. The corresponding sodium thiolates, however, break up the $Rh_2(AcO)_4$ framework in the presence of O_2 to form an oligomeric chain of triply S-bridged Rh(III) ions, each with six Rh—S (2.36 ± 0.02 Å) bonds. The $Rh^{III}\cdots Rh^{III}$ distance, 3.18 ± 0.02 Å, in the chain is similar to that previously found for the aerobic reaction product from aqueous solutions of $Rh_2(AcO)_4$ and glutathione (H_3A), $\{Na_2[Rh_2^{III}(HA)_4]\cdot 7H_2O\}_n$, in which each Rh(III) ion is surrounded by about four Rh—S (2.33 ± 0.02 Å) and about two Rh—O (2.08 ± 0.02 Å). The reaction products obtained in this study can be used to predict how dirhodium(II) tetracarboxylates would react with cysteine-rich proteins and peptides, such as metallothioneins.

1. Introduction

Dirhodium(II) tetracarboxylates $[Rh_2(RCOO)_4]$ are compounds with specific applications in biological and chemical systems due to the stability of their Rh_2^{4+} core, resulting from the single Rh—Rh bond supported by four carboxylate bridges in a 'lantern' structure. Their anti-tumor activity was initially reported by the Bear group (Erck *et al.*, 1974; Bear *et al.*, 1975). They also function as catalysts, especially with chiral ligands *R* that promote enantioselectivity and chemoselectivity in carbene insertion reactions into C—H bonds, such as cyclopropanation and C—H functionalization (Hansen & Davies, 2008), or insertion into polar *X*—H (*X* = S, N, O, *etc.*) bonds (Miller & Moody, 1995; García *et al.*, 1996; Zhang *et al.*, 2003). Reactions involving this family of compounds generally start with the formation of an adduct by a nucleophilic ligand *L* (Lewis base) coordinating in a monodentate manner to the axial positions, $[Rh_2(RCOO)_4L_{1-2}]$ (see **1** in Fig. 1) (Chifotides & Dunbar, 2005). For example, $[Rh_2^{4+}]$-carbenoids are expected to form in the initial step of the above catalytic insertion reactions (García *et al.*, 1996; Zhang *et al.*, 2003). While the axial ligands are labile and easily exchanged, the bridging carboxylate groups are kinetically inert (Bear *et al.*, 1979), and their substitution is proposed to occur stepwise. After an initial axial coordination of, for example, (N/O)-donor ligands with chelating (*e.g.* bipyridine) and/or bridging ability (*e.g.*

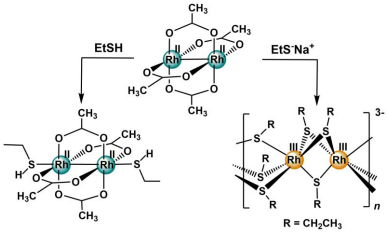

guanine), the probable next step is formation of axial–equatorial (*ax–eq*) and finally *eq–eq* bonds (Yoshimura *et al.*, 2003; Chifotides *et al.*, 2004; Dunbar *et al.*, 1994; Deubel & Chifotides, 2007). It has been suggested that the biological activity of dirhodium(II) carboxylates requires easily accessible axial positions (Aguirre *et al.*, 2007).

Dirhodium(II) tetracarboxylates form adducts with nearly all common donor atoms, including sulfur (Chifotides & Dunbar, 2005). While the thiol (—SH) functional group is important both from biological and chemical points of view, structural information for reaction products of thiols and thiolates with dirhodium(II) carboxylates is limited. Such information would be useful, for example, in elucidating reactions of this family of anti-tumour active compounds with thiol-containing biomolecules, and have prompted several studies (Erck *et al.*, 1976; Howard *et al.*, 1976, 1977; Pneumatikakis & Psaroulis, 1980; Jakimowicz *et al.*, 2000; Sorasaenee *et al.*, 2002, 2003; Wong & Stillman, 2016; Wong *et al.*, 2017; Jalilehvand *et al.*, 2017; Enriquez Garcia & Jalilehvand, 2018).

The only reported crystal structures for such compounds are those of $Rh_2(AcO)_4$ (**1**, $AcO^- = CH_3COO^-$) with axially coordinated benzylthiol or thiophenol groups (Christoph & Tolbert, 1980; Felthouse, 1982). Using combined data from different techniques such as electrospray ionization mass spectrometry (ESI-MS) and extended X-ray absorption fine-structure (EXAFS) spectroscopy, we recently reported that the aerobic reactions of $Rh_2(AcO)_4$ with cysteine (H_2Cys) and glutathione (GSH; denoted H_3A in its triprotonated form) in aqueous media at physiological pH result in the formation of oligomeric products $\{Na_2[Rh^{III}_2(S,N\text{-Cys})_4]\cdot 5H_2O\}_m$ and $\{Na_2[Rh^{III}_2(S\text{-HA})_4]\cdot 7H_2O\}_n$ (*i.e.* Rh^{III}–GSH; **2** in Fig. 1), with two and three thiolate groups, respectively, bridging between the two Rh(III) ions (Jalilehvand *et al.*, 2017; Enriquez Garcia & Jalilehvand, 2018). Also, at early stages of the reaction between $Rh_2(AcO)_4$ and penicillamine (3,3′-dimethylcysteine) at the pH of mixing (~3.0), we detected ESI-MS peaks corresponding to $[Rh^{II}_2(AcO)_4(HPen)]^-$, $[Rh^{II}_2(AcO)_4(Pen)]^{2-}$ and $[Rh^{III}_2(AcO)_4(HPen)_2]^{2-}$ ions, and also made similar observations for the reaction with *N*-acetylcysteine (H_2NAC). Therefore, we proposed that *two* deprotonated thiol groups are needed to oxidize the Rh(II) ions to Rh(III) (Jalilehvand *et al.*, 2017).

Wong *et al.* in another recent study, based on ESI-MS and density functional theory (DFT) calculations, suggested that, when $Rh_2(AcO)_4$ reacts with excess glutathione in aqueous solution under anaerobic conditions, deprotonated glutathione (GS^-) binds to the axial positions of $Rh_2(AcO)_4$ to form $[Rh^{II}_2(AcO)_4(GS)(H_2O)]^-$ and $[Rh^{II}_2(AcO)_4(GS)_2]^{2-}$ complexes (Wong *et al.*, 2017). They also proposed that $Rh_2(AcO)_4$ releases all carboxylate ligands when reacting with the β-domain of human metallothionein (β-MT) 1a under anaerobic conditions. According to the authors the metallated Rh^{II}_2-β-MT retains the Rh—Rh bond 'with each Rh replacing four of the cysteine thiol protons', creating a square pyramidal coordination geometry around each Rh(II) ion in the dirhodium core (Wong & Stillman, 2016). However, Sorasaenee *et al.* showed that the anaerobic reaction of $[Rh^{II}_2(AcO)_2(bpy)_2(CH_3CN)_2](BF_4)_2$ (**3**) (bpy = 2,2′-bipyridine) with excess of the monodentate ligand sodium benzylthiolate, NaC_6H_5S, led to formation of a dirhodium(II) complex $[Rh^{II}(\mu\text{-}S\text{-}C_6H_5S)(\eta^1\text{-}S\text{-}C_6H_5S)(bpy)]_2\cdot CH_3OH$ (**4**), with two bridging thiolates and another two thiolates opposite the Rh—

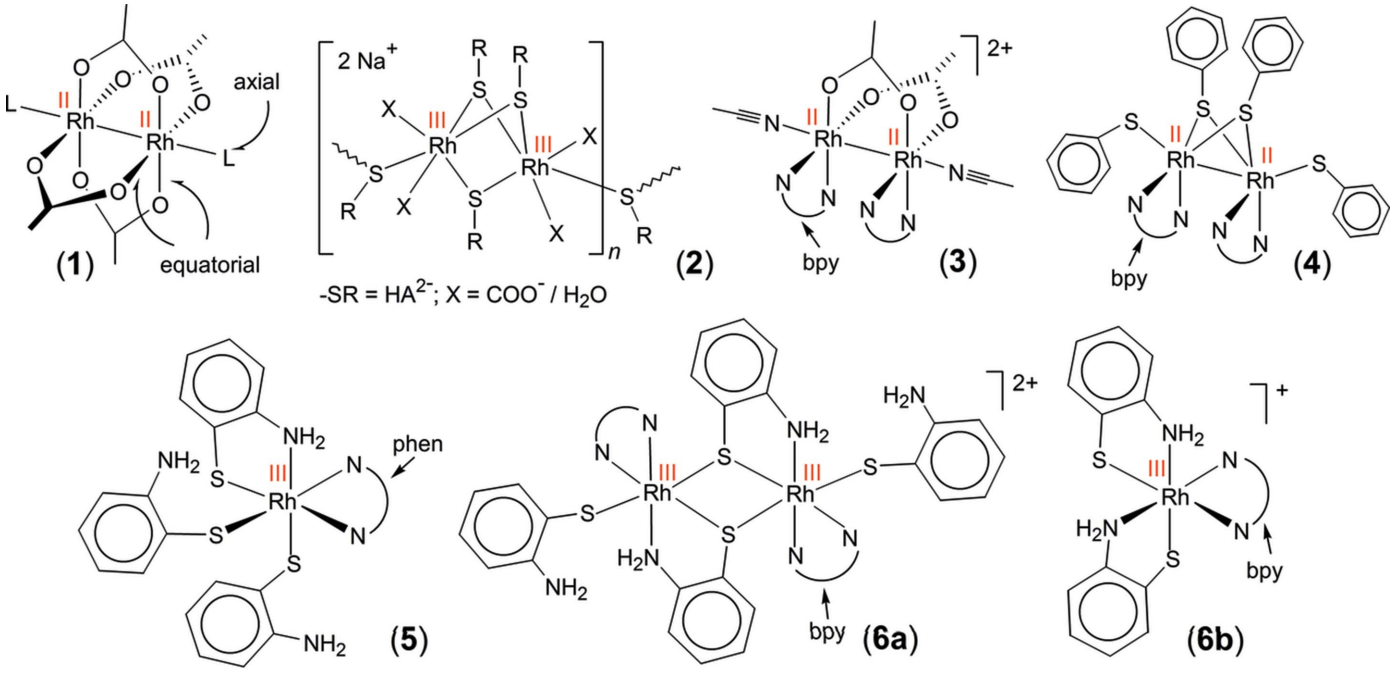

Figure 1
Structures of $[Rh^{II}_2(AcO)_4]$ (**1**), $\{Na_2[Rh^{III}_2(S\text{-HA})_4].7H_2O\}_n$ (*i.e.* Rh^{III}–GSH) (**2**), $[Rh^{II}_2(AcO)_2(bpy)_2(CH_3CN)_2]^{2+}$ (**3**), $[Rh^{II}(\mu\text{-}S\text{-}C_6H_5S)(\eta^1\text{-}S\text{-}C_6H_5S)(bpy)]_2$ (**4**), $[Rh^{III}(\eta^2\text{-}C_6H_7NS)(\eta^1\text{-}C_6H_7NS)_2(phen)]$ (**5**), $[Rh^{III}(\mu\text{-}S,N\text{-}C_6H_6NS)(\eta^1\text{-}S\text{-}C_6H_6NS)(bpy)]^{2+}_2$ (**6a**) and $[Rh^{III}(S,N\text{-}C_6H_6NS)_2(bpy)]^+$ (**6b**); see text, and Enriquez Garcia & Jalilehvand (2018), Sorasaenee *et al.* (2002, 2003).

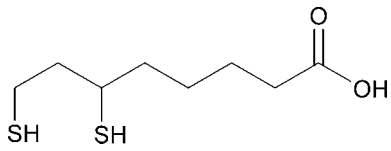

Figure 2
Dihydrolipoic acid (DHLA).

Rh bond (see Fig. 1). The authors described this reaction as 'an important first step in understanding the metabolism of dirhodium anticancer compounds with thiol-containing peptides and proteins' (Sorasaenee *et al.*, 2003).

Sorasaenee *et al.* also reported that the aerobic reaction of a similar complex $[Rh^{II}_2(AcO)_2(phen)_2(CH_3CN)_2](PF_6)_2$ (phen = 1,10-phenanthroline) with excess 2-aminothiophenol (C_6H_7NS, a ligand with chelating ability) resulted in a mononuclear complex, $[Rh^{III}(\eta^2\text{-}C_6H_7NS)(\eta^1\text{-}C_6H_7NS)_2(phen)]$ (**5**), while the aerobic reaction of complex **3** with four-fold C_6H_7NS yielded both mono- and bi-nuclear Rh(III) complexes, $[Rh^{III}(\mu\text{-}S,N\text{-}C_6H_6NS)(\eta^1\text{-}S\text{-}C_6H_6NS)(bpy)]_2^{2+}$ (**6a**) and $[Rh^{III}(S,N\text{-}C_6H_6NS)_2(bpy)]^+$ (**6b**), co-crystallized in the same unit cell (Sorasaenee *et al.*, 2002). The presence of the (N—N) ligands bpy and phen have probably promoted the formation of the monomeric Rh(III) species **5** and **6b** (Jalilehvand *et al.*, 2017). No crystal structure has been reported for reaction product(s) of dirhodium(II) tetracarboxylate with thiolates.

Our goal in the current study was to gain better understanding of the structural changes that occur around the rhodium ions when dirhodium(II) tetracarboxylates $[Rh_2(RCOO)_4]$ react with thiols and thiolates under aerobic conditions. For this purpose, we used X-ray absorption spectroscopy to investigate reactions of $Rh_2(AcO)_4$ with two thiol-containing ligands ethanethiol (C_2H_5SH) and dihydrolipoic acid (DHLA) and also with their sodium thiolate salts. We chose the dithiol molecule DHLA (Fig. 2) to explore whether a molecule that can form an *S,S*-chelate with metal ions (Ioannou & Tsivgoulis, 2014) would facilitate the breakdown of the $Rh_2(AcO)_4$ structure under aerobic conditions. We have previously compared such an effect for cysteine, which behaves as an (*S,N*)- or (*S,N,O*)-donor ligand in its reaction product with $Rh_2(AcO)_4$, with *N*-acetylcysteine that prefers to bind as a monodentate thiolate ligand rather than forming a *S,O*-chelate (Jalilehvand *et al.*, 2017). In the current study, we also performed time-dependent density functional theory (TD-DFT) calculations to explain the observed shifts in the UV–vis absorption spectra of $Rh_2(AcO)_4$ when dissolved in ethanethiol.

2. Experimental section

Sodium hydroxide, ethanethiol (EtSH), sodium ethanethiolate (NaEtS), (±)-α-lipoic acid (LA) were used without further purification. Dirhodium(II) tetraacetate was used as supplied by Pressure Company Co. Extra dry oxygen (99.6%) was supplied by Praxair. Dihydrolipoic acid (DHLA) and its sodium dithiolate salt Na_3(DTLA) were prepared according to literature procedures (Spuches *et al.*, 2005; Kubicki *et al.*, 1995). Methanol (MeOH) was dried by refluxing twice over magnesium turnings under argon atmosphere, whereas dry tetrahydrofuran (THF) was obtained by refluxing over sodium/benzophenone and distilling immediately before use. Ethanol (EtOH) was degassed by passing argon through a boiled solution until cooled down to room temperature. Rhodium analysis was performed by the Canadian Microanalytical Services Ltd.

2.1. Sample preparation

2.1.1. Synthesis of Na_3(DTLA). Sodium metal (24.0 mmol) was added to a transparent solution of DHLA (4.80 mmol) in dry THF (20.0 ml) under argon atmosphere. The mixture was refluxed (70°C) under a stream of argon for 24 h. A white precipitate was formed, which was filtered under inert atmosphere and washed with THF (Kubicki *et al.*, 1995). The solid was stored in a glove box to avoid decomposition.

2.1.2. Solutions of $Rh_2(AcO)_4$ in ethanethiol, $Rh_2(AcO)_4(EtSH)_2$ (7). Dissolution of $Rh_2(AcO)_4$ (0.125 mmol) in 2.50 ml ethanethiol (33.8 mmol, d = 0.839 g ml^{-1}) resulted in a clear burgundy solution after 30 min stirring under a stream of argon gas to prevent thiol (—SH) oxidation to disulfide (—S—S—); this solution was used for the EXAFS data collection (C_1 = 50 m*M*). For UV–vis measurement, a dilute solution (C_1 = 5.0 m*M*) was prepared by dissolving $Rh_2(AcO)_4$ (0.0025 mmol) in 0.50 ml neat ethanethiol. Another UV–vis spectrum was collected for a 1.0 m*M* solution of $Rh_2(AcO)_4$ (0.050 mmol) dissolved in 50.0 m*M* ethanethiol in chloroform (total volume = 50.00 ml). The solutions were kept under aerobic conditions prior to, or during, the physical measurements.

2.1.3. $[Rh_2(AcO)_4(DHLA)]_n$ solid (8). To a DHLA solution (0.904 mmol) in 5.0 ml EtOH, a suspension of $Rh_2(AcO)_4$ (0.226 mmol) in 15.0 ml EtOH was added dropwise, resulting in a blue–green solution. The reaction was carried out under a stream of argon in O_2-free solvent to avoid oxidation of thiol groups. After 24 h of stirring at room temperature a violet precipitate formed that was filtered in air, washed with EtOH and dried in a desiccator under vacuum. The solid was insoluble in common solvents. Calcd. for $[Rh_2(AcO)_4(DHLA)]_n$ $(Rh_2C_{16}H_{28}O_{10}S_2)_n$: C, 29.55; H, 4.34. Found: C, 29.81; H, 4.34; N, 0.02.

2.1.4. Aerobic reaction of $Rh_2(AcO)_4$ with sodium ethanethiolate (NaEtS) and Na_3(DTLA), the sodium dithiolate salt of DHLA (9 and 10). A solution of the sodium thiolate salt (2.26 mmol) in 10.0 ml of dry MeOH was added dropwise to a completely dissolved solution of $Rh_2(AcO)_4$ (0.226 mmol) in 180.0 ml dry MeOH under a stream of argon. Dry MeOH was used to avoid protonation of the sodium salts. The solution immediately turned dark orange–red and a precipitate was observed after 2 h. After stirring for 24 h, dry O_2 was vigorously bubbled through the reaction mixture for 15 min, and stirring continued under O_2 atmosphere for another 24 h. The reaction mixture was concentrated to 5 ml and the precipitate filtered off and then re-suspended in a 10.0 ml water–methanol (1:1) mixture to wash away any sodium acetate

residue. The suspension was filtered to collect the orange precipitate, which was washed with distilled water and methanol and then dried under vacuum. The solid product was diamagnetic and insoluble in water and most organic solvents. Found for the Rh(III) ethanethiolate product (**9**): C, 24.02; H, 4.93; S, 23.80; Rh, 31.49. Elemental analysis calculations were carried out for several combinations of Rh(III), $CH_3CH_2S^-$, Na^+ and CH_3COO^-, and the composition closest to the experimental data was $[Na_3Rh_7(C_2H_5S)_{17}(CH_3COO)_7(H_2O)_4]_n$ $(Na_3Rh_7C_{48}H_{114}O_{18}S_{17})_n$: C, 24.92; H, 4.97; S, 23.56; Rh, 31.13. Compound **10** is also an oligomer (or polymer) with similar structure as **9** (see below).

2.2. Methods

Magnetic susceptibility measurements on the solid samples were performed using a Johnson Matthey magnetic susceptibility balance.

2.2.1. Electronic spectroscopy. A Cary 300 UV–vis double-beam spectrophotometer was used to measure the UV–vis spectra of $Rh_2(AcO)_4$ in water (C_1 = 1.0 m*M*), in neat ethanethiol (C_1 = 5.0 m*M*), or in 50.0 m*M* ethanethiol in chloroform (C_1 = 1.0 m*M*), using the corresponding solvents as blank, with 1 mm path length quartz cells as sample holder, and 1.0 nm energy resolution.

2.2.2. Vibrational spectroscopy. The IR spectrum of a KBr disc of the $[Rh_2(AcO)_4(DHLA)]_n$ solid (**7**) was measured using a Thermo Nicolet NEXUS 470 FT-IR ESP spectrometer (4 cm^{-1} resolution). The IR spectrum of pure DHLA was obtained by placing a drop of DHLA (oil) between two BaF_2 disks (window cut-off 870 cm^{-1}).

2.2.3. X-ray absorption spectroscopy: data collection. Rh *K*-edge X-ray absorption spectra were measured at room temperature at BL7-3 (500 mA) at the Stanford Synchrotron Radiation Lightsource (SSRL) operating under 3 GeV. Higher-order harmonics were rejected by detuning a Si(220) (ϕ = 0°) double-crystal monochromator to 50% of maximum intensity (I_0) at the end of the Rh *K*-edge scan range. The ion chambers (I_0, I_1 and I_2) were filled with nitrogen (N_2) and the Lytle detector with argon (Ar). The X-ray energy was internally calibrated by assigning the first inflection point in the absorption spectrum of a Rh foil (placed between the I_1 and I_2 ion chambers) to 23219.80 eV. The monochromator energy step in the X-ray absorption near-edge structure (XANES) region was 0.3 eV. The solution of $[Rh_2(AcO)_4(EtSH)_2]$ (**7**) was held inside a 2 mm pinhole sample holder with Kapton windows, collecting the data at 120 K to suppress the strong odour of EtSH (boiling point = 308 K; freezing point = 125 K). The solid samples **1**, **8**, **9** and **10** were mixed with boron nitride (sample: BN = 70:30 *w*/*w*), finely ground and pressed in a 1 mm Al frame with Mylar tape as window material. Five to seven scans were collected for each sample in transmission mode (except for **1**, which was measured in fluorescence mode). All individual scans were compared prior to averaging to ensure that no radiation damage occurred during measurement.

2.2.4. X-ray absorption spectroscopy: data analysis. EXAFS oscillations were extracted using the *WinXAS3.1* program (Ressler, 1998), by removing a first-order polynomial background in the pre-edge region, followed by edge step normalization. The threshold energy (E_0), defined as the first inflection point in the absorption edge, varied over a narrow range: 23226.0 eV (for **1**), 23225.8 eV (**7**), 23225.6 eV (**8**), 23225.4 (**9**), 23225.3 (**10**). The E_0 value was used for converting the energy unit to photoelectron wavevector, k (Å^{-1}), where $k = [(8\pi^2 m_e/h^2)(E - E_0)]^{1/2}$. The EXAFS oscillation was then extracted by removing the atomic background absorption above the edge, using a seven-segment cubic spline.

For modelling theoretical EXAFS oscillations, $\chi(k)$, the *FEFF7.0* program (Zabinsky *et al.*, 1995; Ankudinov & Rehr, 1997) was used to obtain *ab initio* calculated amplitude $f_{\rm eff}(k)_i$, phase shift $\phi_{ij}(k)$, and mean free path $\lambda(k)$ functions [equation (1)] for coordination models obtained from the crystal structures of $[Rh_2(AcO)_4(H_2O)_2]$ (Cotton *et al.*, 1971), $\{Rh_2(AcO)_4[(PhCH_2)_2S]_2\}$ (Cambridge Structural Database (CSD) code: DEHBIB) (Clark *et al.*, 1985) and ΔΛ-[Rh{Ir(aet)$_3$}$_2$]Br$_3$ (CSD: AQUVOX; Haet = 2-aminoethanethiol) (Mahboob *et al.*, 2004), as well as the optimized geometry for $[Rh_4(EtS)_{15}]^{3-}$ (see the supporting information),

$$\chi(k) = \sum_i \frac{N_i S_0^2(k)}{kR_i^2} \left| f_{\rm eff}(k) \right|_i \exp\left(-2k^2\sigma_i^2\right) \times \exp\left[-2R_i/\lambda(k)\right] \sin\left[2kR_i + \phi_{ij}(k)\right]. \quad (1)$$

The input file for the *FEFF* program was created by the *ATOMS* program (Ravel, 2001), using the atomic coordinates of the above crystal structures. For the ΔΛ-[Rh{Ir(aet)$_3$}$_2$]Br$_3$ structure the terminal Ir atoms were replaced by Rh in the *ATOMS* input file, because of their similar ionic radii, Rh(III) 0.665 Å and Ir(III) 0.68 Å (Shannon, 1976).

The least-squares curve-fitting of the k^3-weighted model function $\chi(k)$ to the experimental unfiltered EXAFS oscillation was performed over the k-range 2.8–18 Å^{-1}. For each backscattering path around the central Rh atom, the distance (R), the Debye–Waller factor parameter (σ^2) and in some cases the coordination number (N) were refined, while ΔE_0 was refined as a common value for all scattering paths in the model. The amplitude reduction factor (S_0^2) was refined to 0.92 for **1** and fixed at this value for all other fittings. The accuracy of bond distances, σ^2 and refined N values is within ±0.02 Å, ±0.001 Å^2 and ±10–15%, respectively.

2.2.5. XANES calculations. The Rh *K*-edge XANES simulations were performed by means of the *FEFF8.10* program (Ankudinov *et al.*, 1998), using the atomic coordinates of the DFT optimized geometries of $[Rh_2(AcO)_4(EtSH)_2]$ and $[Rh_4(SEt)_{15}]^{3-}$ and muffin-tin potentials with 15% overlap. The best results were obtained when the Hedin–Lundqvist exchange-correlation potential was used for the excited state. The input files for both XANES calculations are presented in the supporting information.

2.2.6. Computational calculations. The electronic structure calculations were performed using the *Gaussian09* package (Frisch *et al.*, 2016). Initial atomic coordinates were imported

from the crystal structure of $[Rh_2(AcO)_4(H_2O)_2]$ (Cotton *et al.*, 1971), and were used as the starting point for the geometry optimizations. The Becke–Half-and-Half–LYP density functional was employed with the 6-31G(d) basis set for all non-metal atoms and the LANL2DZ pseudopotential for the Rh atoms. All calculated vibrational frequencies for the optimized geometries were positive. The optimized geometry of $[Rh_2(AcO)_4(H_2O)_2]$ in its ground state was compared with the reported crystal structure (Cotton *et al.*, 1971) to test the combination of functional and basis sets. All Rh—Rh and Rh—O_{eq} distances in the optimized geometry were within ±0.02 Å of those in the crystal structure.

TD-DFT calculations were performed for the optimized geometries of $[Rh_2(AcO)_4(H_2O)_2]$, $[Rh_2(AcO)_4(H_2S)_2]$ and $[Rh_2(AcO)_4(EtSH)_2]$ placed inside a solvent cavity, considering the first 100 lowest vertical excitations. The solvent effects were described by means of the Polarizable Continuum Model (PCM) (Frisch *et al.*, 2016), using water for all three systems, and also chloroform for $[Rh_2(AcO)_4(EtSH)_2]$.

The optimization and TD-DFT calculations were repeated using the same functional, but this time with the 6-311++G(2d,p) basis set, including the LANL2TZ(f) pseudopotential for Rh, to study whether this more comprehensive and flexible combination of basis sets would significantly affect the results. Both models resulted in similar optimization parameters and transition energies, and identity of the excitations, with comparable TD-DFT-reported state compositions in terms of fractional contributions to the excitations. These results suggest that the original combination of basis sets describes the system adequately.

3. Results and discussion

3.1. Electronic absorption spectroscopy

The UV–vis spectrum of the emerald green aqueous solution of $Rh_2(AcO)_4$ (**1**) showed the characteristic broad band of $[Rh_2(AcO)_4(H_2O)_2]$ with λ_{max} = 584 nm (Boyar & Robinson, 1983), which previously has been attributed to a $\pi^*(Rh_2^{4+}) \rightarrow \sigma^*(Rh_2^{4+})$ transition (band **I**); see Fig. 3 (Wilson & Taube, 1975; Norman *et al.*, 1979; Norman & Kolari, 1978). Schematic molecular orbital (MO) diagrams for the dirhodium(II) core, with calculated energy levels of $Rh_2(AcO)_4$ and $[Rh_2(AcO)_4(H_2O)_2]$ are shown in Figs. S1*a*, S1*b* and S2*a*, respectively, of the supporting information. The $\pi^*(Rh_2^{4+}) \rightarrow \sigma^*(Rh_2^{4+})$ transition is sensitive to the nature of the donor atom in the axially coordinated ligands (L) in the $[Rh_2(AcO)_4L_2]$ complexes, shifting to shorter wavelength in the following order: O < S < N_{sp3} < N_{sp2} < S = O (Kitchens & Bear, 1969). Burgundy solutions with λ_{max} = 555 nm (blue shift ∼29 nm) are obtained when dissolving $Rh_2(AcO)_4$ in neat ethanethiol (C_1 = 5.0 m*M*), or in 50.0 m*M* ethanethiol in chloroform (C_1 = 1.0 m*M*); see Fig. 3.

This blue shift for band **I** is smaller than those observed for the bis(thioether) adducts of $Rh_2(AcO)_4$ with methionine (λ_{max} = 537 nm) (Chen & Kostic, 1988; Jakimowicz *et al.*, 2000), diethylsulfide (541 nm) (Kitchens & Bear, 1969) and dibenzylsulfide (546 nm) (Clark *et al.*, 1985). The largest shift reported is for the *S*-coordinated dimethylsulfoxide (DMSO) adduct (λ_{max} = 497 nm) (Kitchens & Bear, 1969; Johnson *et al.*, 1963). Dubicki & Martin proposed based on a self-consistent charge and configuration molecular orbital (SCCC-MO) calculation that such blue shifts relative to $[Rh_2(AcO)_4(H_2O)_2]$ are probably caused by an increasing axial interaction between the ligands, *i.e.* the soft S atom of the axial thioether/thiol groups and the $\sigma^*(Rh_2^{4+})$ orbital of the soft Rh(II) ions, which has a high $4d_{z2}$ contribution and is directed toward the ligands L along the linear L—Rh—Rh—L axis. The stronger the ligand field of the axial ligand L, the higher the energy of the antibonding $\sigma^*(Rh_2^{4+})$ orbital (Dubicki & Martin, 1970). The observed colour change should therefore be due to the influence of the axial ethanethiol ligands on the $\pi^*(Rh_2^{4+}) \rightarrow \sigma^*(Rh_2^{4+})$ transition in its $Rh_2(AcO)_4$ adduct (also see Section 3.2) (Felthouse, 1982; Dubicki & Martin, 1970). The retention of the Rh—Rh bond in the ethanethiol adduct of $Rh_2(AcO)_4$ is further confirmed by EXAFS spectroscopy (see below).

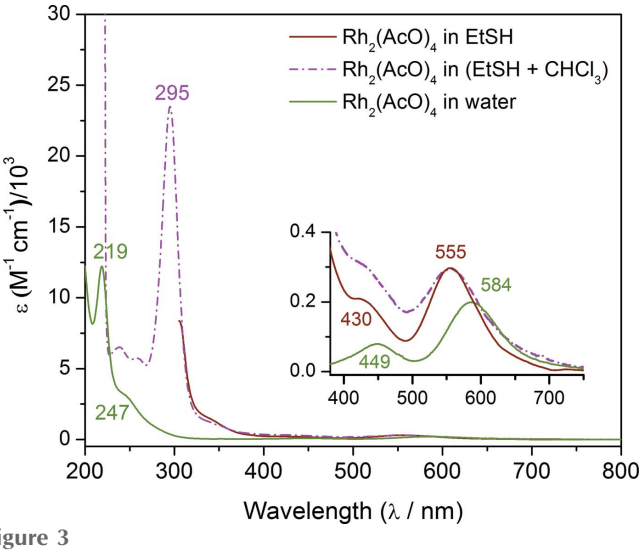

Figure 3
UV–vis spectra of $Rh_2(AcO)_4$ (**1**) dissolved in water (C_1 = 1.0 m*M*), in neat ethanethiol (EtSH, C_1 = 5.0 m*M*; cut-off at ∼300 nm due to high solvent absorption), or in 50.0 m*M* EtSH in chloroform ($CHCl_3$, C_1 = 1.0 m*M*; cut-off at ∼230 nm). Δε = absorption difference between sample and solvent (blank).

Because of the high solvent absorption in neat ethanethiol below ∼300 nm, we also measured the UV–vis spectrum of $Rh_2(AcO)_4$ dissolved in 50.0 m*M* ethanethiol in chloroform (C_1 = 1.0 m*M*), which enabled us to observe an intense band at 295 nm. A similar absorption has been observed at 308 nm in the UV–vis spectra of the bis(thioether) adducts of **1**: $[Rh_2(AcO)_4\{S(CH_2Ph)_2\}_2]$ (Clark *et al.*, 1985) and $[Rh_2(AcO)_4\{methionine\}_2]$ (Chen & Kostic, 1988; Enriquez Garcia *et al.*, 2018).

3.2. Computational studies

To interpret the observed UV–vis absorption bands, DFT calculations were performed followed by TD-DFT calculations. As a starting point for the optimizations, the molecular structure of the aqua complex was adapted from the crystal

structure of $[Rh_2(AcO)_4(H_2O)_2]$ (Cotton *et al.*, 1971); see Section 2.2.6. Then the aqua oxygen atoms were replaced with sulfur to obtain $[Rh_2(AcO)_4(H_2S)_2]$ in order to investigate the effect of the axial donor atom. This was followed by replacing one hydrogen atom of each H_2S ligand with an ethyl group to obtain $[Rh_2(AcO)_4(EtSH)_2]$. The calculated energy diagrams of the MOs for $[Rh_2(AcO)_4L_2]$ (L = H_2O, H_2S and EtSH) are shown in Fig. 4 and the corresponding graphic representations of each molecular orbital are displayed in Figs. S2*a*–S2*c*.

The energies of the calculated MOs for $[Rh_2(AcO)_4(H_2O)_2]$ are in agreement with those calculated by Wong *et al.*, using the CAM-B3LYP functional (Wong *et al.*, 2017). Fig. 4 shows that by changing H_2O to H_2S as the axial ligand the energy of the $\sigma(Rh_2^{4+})$ MO increases. Note that this orbital has some contribution from the $\sigma^*(Rh-X)$ orbital, originating from the axially coordinated donor atom X (*i.e.* O or S), beside the Rh—Rh σ interaction (Sowa *et al.*, 1983). Therefore, the increase in σ bonding interaction between the soft sulfur and Rh(II) atoms will also increase the σ^*(Rh—S) contribution and destabilizes the $\sigma(Rh_2^{4+})$ MO orbital in $[Rh_2(AcO)_4(H_2S)_2]$. Replacing one hydrogen atom in H_2S with an ethyl group in $[Rh_2(AcO)_4(EtSH)_2]$ increases the σ^*(Rh—S) contribution and raises the energy of the $\sigma(Rh_2^{4+})$ orbital further.

The TD-DFT calculations were performed for $[Rh_2(AcO)_4(EtSH)_2]$ in a cavity surrounded by a continuum corresponding to either water or chloroform, to simulate the effect of the experimental conditions (see Section 2.2.6). The resulting calculated transition energies for $[Rh_2(AcO)_4(EtSH)_2]$ were very similar (see Fig. S3) and only the results for water will be discussed hereafter.

The TD-DFT calculations show two excitations with weak oscillator strength ($f \simeq 0.003$–0.004) at 514 nm for $[Rh_2(AcO)_4(EtSH)_2]$ corresponding to the $\pi^*(Rh_2^{4+}) \rightarrow \sigma^*(Rh_2^{4+})$ transition (with ~76% contribution) originating from the two $\pi^*(Rh_2^{4+})$ orbitals (see Fig. S4). This transition is blue-shifted 27 nm compared with the aqua complex (541 nm). The extent of this blue shift is in agreement with the 29 nm blue shift of band **I** observed experimentally for the solutions of **1** dissolved in water and ethanethiol (see Fig. 3). This blue shift was previously described as due to destabilization of the $\sigma^*(Rh_2^{4+})$ MO when the ligand field of the axial ligand increased, moving the $\pi^*(Rh_2^{4+}) \rightarrow \sigma^*(Rh_2^{4+})$ transition toward higher energies (Dubicki & Martin, 1970). However, our DFT calculations show the $\sigma^*(Rh_2^{4+})$ MO energy to be slightly lower in the ethanethiol adduct than in the aqua complex (Fig. 4), suggesting that this $\pi^*(Rh_2^{4+}) \rightarrow \sigma^*(Rh_2^{4+})$ transition, although predominant, is not the only contributing factor to the blue shift of band **I**. In the UV region, our computational results for $[Rh_2(AcO)_4(EtSH)_2]$ show two vertical excitations with high oscillator strength ($f \geq 0.3$) in the 280–290 nm region (Fig. S4). The MO transition that contributes significantly to both excitations is $\sigma(Rh_2^{4+}) \rightarrow \sigma^*(Rh_2^{4+})$, depicted in Fig. 4. Similar calculations for the aqua complex $[Rh_2(AcO)_4(H_2O)_2]$ imply a high contribution (70%) of the same transition to the band at 239 nm (Fig. S2*a* and Table S1). The UV band shift to longer wavelengths for the thiol-coordinated adduct $[Rh_2(AcO)_4(EtSH)_2]$ relative to that of the aqua complex corresponds to the destabilization of the $\sigma(Rh_2)$ orbital. The increase in its energy level leads to a decrease in the energy of the $\sigma(Rh_2^{4+}) \rightarrow \sigma^*(Rh_2^{4+})$ excitation and absorption at longer wavelengths. A second transition with significant contribution to the oscillator strength (38%) is from one of the $\pi(Rh_2^{4+})$ orbitals to the $\sigma^*(Rh_2^{4+})$, as shown in Figs. 4 and S4.

Thus, our TD-DFT calculations for $[Rh_2(AcO)_4(EtSH)_2]$ show that the electronic transitions $\pi(Rh_2^{4+}) \rightarrow \sigma^*(Rh_2^{4+})$ and $\sigma(Rh_2^{4+}) \rightarrow \sigma^*(Rh_2^{4+})$ closely match the experimentally observed band at 295 nm (see Fig. 3).

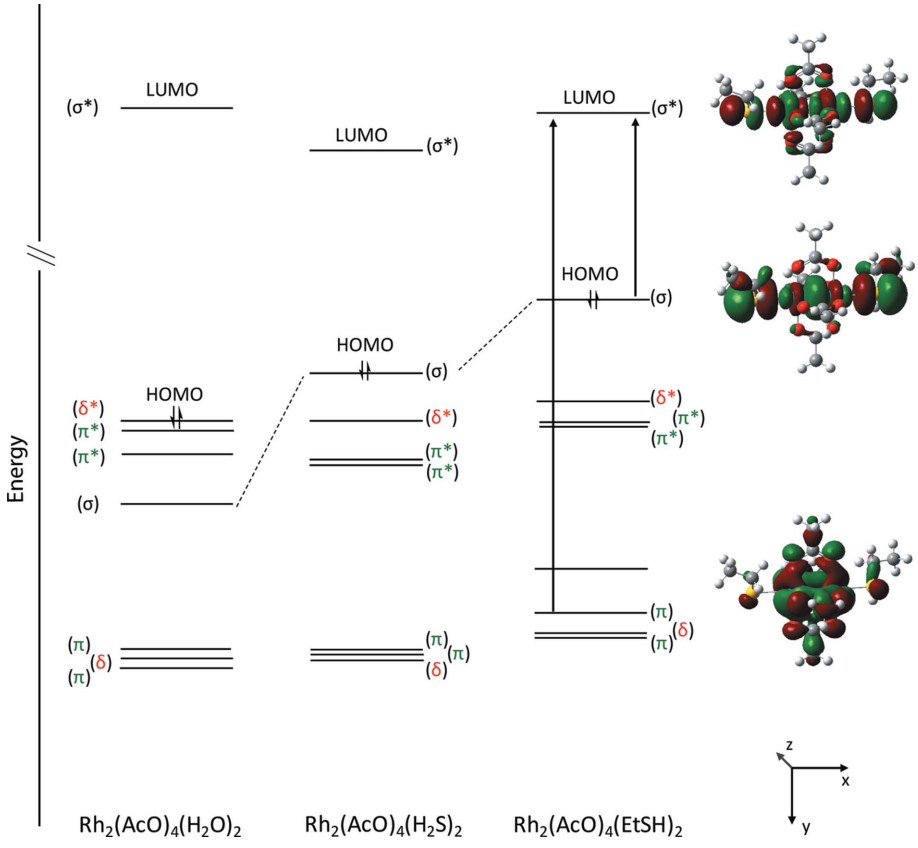

Figure 4
Density functional theory (DFT) calculated energies of the molecular orbitals (MOs) of $[Rh_2(AcO)_4(H_2O)_2]$, $[Rh_2(AcO)_4(H_2S)_2]$ and $[Rh_2(AcO)_4(EtSH)_2]$, and graphic representations of the MOs involved in the $\pi(Rh_2^{4+}) \rightarrow \sigma^*(Rh_2^{4+})$ and $\sigma(Rh_2^{4+}) \rightarrow \sigma^*(Rh_2^{4+})$ transitions, which are the main contributors to the 295 nm band observed in the UV–vis spectrum of a 1.0 m*M* solution of $[Rh_2(AcO)_4(EtSH)_2]$ in 50 m*M* EtSH in chloroform (see Fig. 3).

Note that for the aqua complex $[Rh_2(AcO)_4(H_2O)_2]$ the $\sigma(Rh_2^{4+}) \rightarrow \sigma^*(Rh_2^{4+})$ transition occurs at 247 nm (see Fig. 3) (Norman & Kolari, 1978).

3.3. Rh *K*-edge X-ray absorption spectroscopy

Fig. 5 compares the k^3-weighted Rh *K*-edge EXAFS spectra and the corresponding Fourier transforms (FTs) of solid $Rh_2(AcO)_4$ (**1**) and its solution in ethanethiol, $[Rh_2(AcO)_4(EtSH)_2]$ (**7**), $[Rh_2(AcO)_4(DHLA)]_n$ solid (**8**), as well as the reaction products of $Rh_2(AcO)_4$ with excess amount of the sodium thiolate salts NaEtS (**9**) and Na_3(DTLA) (**10**).

The Fourier transforms of the EXAFS spectra obtained for a solution of $Rh_2(AcO)_4$ in ethanethiol (**7**), and for the $[Rh_2(AcO)_4(DHLA)]_n$ solid (**8**) show a distinct peak for the Rh—Rh bond in a similar position as the corresponding FT peak for $Rh_2(AcO)_4$ in Fig. 5. For the aerobic reaction products of $Rh_2(AcO)_4$ with large excess (mole ratio 1:10) of sodium ethanethiolate (**9**), or the sodium dithiolate salt of DHLA (**10**), the EXAFS oscillations and the corresponding FTs differ considerably from those of $Rh_2(AcO)_4$ as shown in Fig. 5. The EXAFS spectra of products **9** and **10** almost superimpose (Fig. S5). For comparison with the Rh^{III}–GSH product (**2**), see Section 3.3.3.

Changes in the XANES spectra of these compounds are also informative. Fig. 6 (top) displays similar features for solid $Rh_2(AcO)_4$ (**1**) and its solution in ethanethiol $[Rh_2(AcO)_4(EtSH)_2]$ (**7**). However, the XANES spectrum of the reaction product of $Rh_2(AcO)_4$ with excess amount of sodium ethanethiolate (**9**) differs from its solution in ethanethiol (**7**). Thus, a drastic change in the electronic environment around the Rh ions occurs when $Rh_2(AcO)_4$ reacts with sodium ethanethiolate under aerobic conditions.

To some extent the first inflection point (E_0) of the absorption edges is also affected: for the Rh(II) compounds **1** and **7**, the E_0 values are 23226.0 and 23225.8, respectively, while for the Rh(III) compound **9** the first inflection point occurs at slightly lower energy (23225.4 eV). For a higher oxidation state, higher energy is generally expected to excite a core electron. However, in this case, the Rh(III) ions in **9** are surrounded by six electron-rich thiolate groups, which provide electron density to the Rh(III) ions. The calculated Mulliken charge of +0.79 for the Rh(III) ions in Rh_2S_3 (Tan & Harris, 1998), with a similar Rh surrounding as in **9** (Section 3.3.3), is consistent with the lower energy required for exciting core electrons of Rh(III) ions in **9**.

3.3.1. Ethanethiol solution of $Rh_2(AcO)_4$. The Rh *K*-edge EXAFS spectrum of the ethanethiol solution of $Rh_2(AcO)_4$ fits well to a model consisting of four Rh—O (2.03 ± 0.02 Å), one Rh—Rh (2.41 ± 0.02 Å) and one Rh—S (2.52 ± 0.02 Å) distances around each Rh ion; see the spectrum of **7** in Fig. 5 and Table 1. These bond lengths are comparable with the

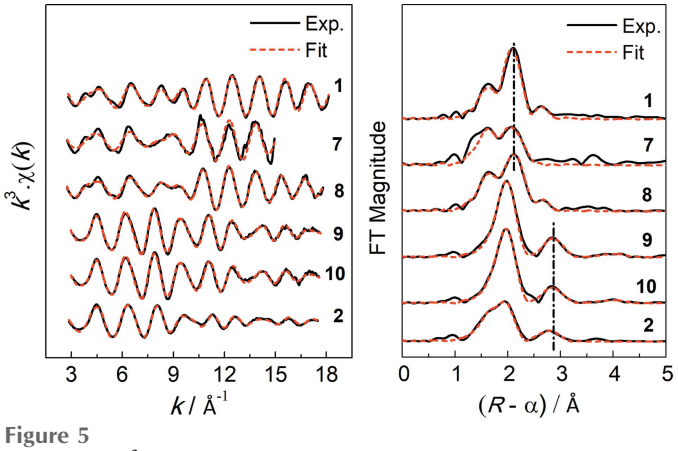

Figure 5
(Left) The k^3-weighted Rh *K*-edge EXAFS spectra, and (right) the corresponding Fourier transforms of: $Rh_2(AcO)_4$ solid (**1**) and its solution in ethanethiol, $[Rh_2(AcO)_4(EtSH)_2]$ (**7**), $[Rh_2(AcO)_4(DHLA)]_n$ solid (**8**), reaction products of $Rh_2(AcO)_4$ with excess of the sodium thiolates NaEtS (**9**) and Na_3(DTLA) (**10**), and concentrated solution of Rh^{III}–GSH product (**2**) with three bridging thiolato groups between the Rh(III) ions (Enriquez Garcia & Jalilehvand, 2018); see below. The curve fitting results are presented in Table 1.

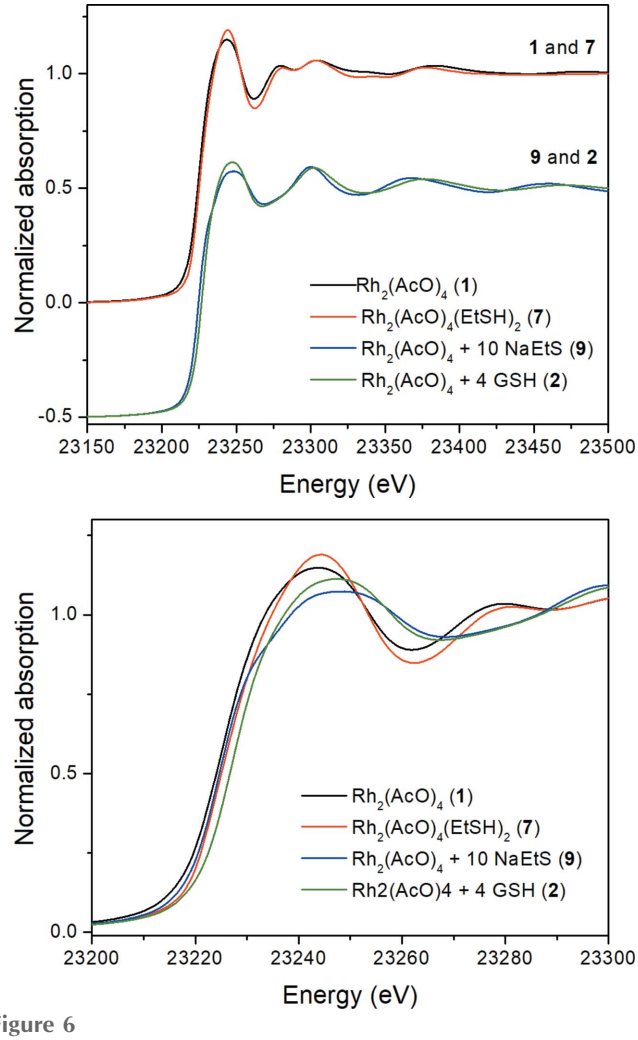

Figure 6
Normalized Rh *K*-edge XANES spectra of: $Rh_2(AcO)_4$ solid (**1**) and its solution in ethanethiol, $[Rh_2(AcO)_4(EtSH)_2]$ (**7**), reaction product of **1** with excess sodium ethanethiolate (NaEtS) (**9**), and solution of Rh^{III}–GSH reaction product (**2**) with three bridging thiolato groups between the Rh(III) ions (Enriquez Garcia & Jalilehvand, 2018). The electronic environment around the Rh ions in **9** clearly differs from **7**, but is rather similar to **2**.

Table 1
Structural parameters derived from least-squares curve-fitting of simulated EXAFS oscillations for models of the local Rh-ion environment to the experimental EXAFS spectra of **1**, **2**, **7**–**10** shown in Fig. 5.

The amplitude reduction factor (S_0^2) was refined to 0.92 for **1** and fixed at this value for all other fittings; *f* = fixed value; estimated errors: $R \pm 0.02$ Å; $\sigma^2 \pm 0.001$ Å^2; $N \pm 10$–15%.

	Rh—O			Rh—S			Rh—Rh / Rh···Rh		
Sample	*N*	*R* (Å)	σ^2 (Å^2)	*N*	*R* (Å)	σ^2 (Å^2)	*N*	*R* (Å)	σ^2 (Å^2)
1†	4*f*	2.03	0.0029				1*f*	2.38	0.0012
7‡	4*f*	2.03	0.0022	1*f*	2.52	0.0050	1*f*	2.41	0.0015
8§	4*f*	2.03	0.0023	1*f*	2.61	0.0082	1*f*	2.41	0.0014
9¶				6.2	2.37	0.0041	1.5	3.18	0.0046
10††				6.3	2.37	0.0044	1.5	3.17	0.0053
2‡‡	2.5	2.08	0.0034	4.1	2.33	0.0050	0.85	3.11	0.0046

† Additional refined paths: 4Rh···C (R = 2.88 Å, σ^2 = 0.0034 Å^2), 4Rh···O'_{eq} (R = 3.09 Å, σ^2 = 0.0057 Å^2). ‡ Additional refined paths: 4Rh···C (R = 2.96 Å, σ^2 = 0.0031 Å^2), 4Rh···O'_{eq} (R = 3.09 Å, σ^2 = 0.0023 Å^2). § Additional refined paths: 4Rh···C (R = 2.88 Å, σ^2 = 0.0030 Å^2), 4Rh···O'_{eq} (R = 3.08 Å, σ^2 = 0.0061 Å^2). ¶ Additional refined path {using *FEFF* files from the optimized geometry of $[Rh_4(EtS)_{15}]^{3-}$}: 6.2Rh—S—Rh—S (n_{leg} = 4; along the linear S—Rh—S entities) (R = 4.73 Å, σ^2 = 0.0087 Å^2), correlating its coordination number to Rh—S. †† Additional refined path: 6.3Rh—S—Rh—S (n_{leg} = 4) (R = 4.72 Å, σ^2 = 0.0097 Å^2), correlating its coordination number to Rh—S. ‡‡ Concentrated solution of Rh^{III}–GSH reaction product with three bridging thiolato groups between the Rh(III) ions (Enriquez Garcia & Jalilehvand, 2018).

Rh—Rh bond lengths 2.4020 (3) Å and 2.4024 (7) Å, and corresponding Rh—S_{axial} distances 2.551 (2) Å and 2.548 (1) Å in the crystal structures of $[Rh_2(AcO)_4(HSCH_2Ph)_2]$ and $[Rh_2(AcO)_4(HSPh)_2]$, respectively (Christoph & Tolbert, 1980; Felthouse, 1982). This result is consistent with a dominating $[Rh_2(AcO)_4(EtSH)_2]$ (**7**) complex in the ethanethiol solution, with EtSH molecules occupying the axial sites of the $Rh_2(AcO)_4$ core (Fig. 7).

The elongation of the Rh—Rh bond distance from 2.38 ± 0.02 Å in solid $Rh_2(AcO)_4$ (**1**) to 2.41 ± 0.02 Å in $[Rh_2(AcO)_4(EtSH)_2]$ (**7**) can be attributed to the *trans* influence of the axially coordinated ethanethiol ligands, and the destabilization of the $\sigma(Rh_2^{4+})$ orbital energy (see Fig. 4, and Section 3.2). For a series of $[Rh_2(AcO)_4L_2]$ complexes [L = pyridine, $NH(Et)_2$, CO, PF_3, $P(OPh)_3$, $P(Ph)_3$, $P(OCH_3)_3$], it has been shown that axial ligands L, both with strong σ-donating (basicity) or with strong π-accepting ability, can weaken and lengthen the Rh—Rh bond. For example, the elongation of the Rh—Rh distance to 2.430 (3) Å in the $[Rh_2(AcO)_4(PF_3)_2]$ complex has been explained as a result of the strong π-acceptance ability of PF_3 to the empty PF σ^*-orbital, despite its weak σ-donation (due to the electronegative F atoms) (Christoph & Koh, 1979; Orpen & Connelly, 1990). So ethanethiol, which is a fairly weak σ-donor but a good π-acceptor (to a σ^*-orbital) (Kraatz *et al.*, 1993), should have a similar effect on the Rh—Rh bond. Christoph & Koh proposed that π-back donation of electrons to the π-acceptor ligands in $[Rh_2(AcO)_4L_2]$ complexes would occur from filled high-energy MO orbitals with π rather than π^* symmetry (since removing electron density from π^* orbitals would strengthen the Rh—Rh bond) (Christoph & Koh, 1979).

3.3.2. Reaction of $Rh_2(AcO)_4$ with dihydrolipoic acid. We have previously shown that the reaction of $Rh_2(AcO)_4$ with cysteine at mole ratio of 1:4 leads to formation of a $\{Rh_2(HCys)_2(Cys)_2 \cdot 4H_2O\}_n$ precipitate at the pH of mixing (pH = 3.2), and to oligomeric $\{Na_2[Rh_2(Cys)_4]\cdot 5H_2O\}_n$ species at pH = 7.4 in which the cysteinate ligands act as (*S,N*)- or (*S,N,O*)-chelates forming dithiolate bridges between two Rh(III) ions (Jalilehvand *et al.*, 2017). Dihydrolipoic acid (DHLA) could act as a dithiol ligand and form an (*S,S*)-chelate upon deprotonation. Therefore, we investigated the reaction of $Rh_2(AcO)_4$ with DHLA in ethanol as solvent, since DHLA is insoluble in water. The product was a violet precipitate, $[Rh_2(AcO)_4(DHLA)]_n$ (**8**), which was not soluble in common solvents (*e.g.* water, alcohols, acetonitrile, *etc.*). Least-squares curve-fitting of its Rh *K*-edge EXAFS spectrum showed a similar Rh—Rh distance (2.41 ± 0.02 Å) to that in $[Rh_2(AcO)_4(EtSH)_2]$ (**7**); see Table 1. Also, a Rh—S scattering path could be fitted at 2.61 ± 0.02 Å, which is slightly longer than that of **7** (2.52 ± 0.02 Å). Fig. 8 displays the separate contributions from different scattering paths used in the EXAFS model fitting of the $[Rh_2(AcO)_4(DHLA)]_n$ solid (**8**).

In the FT-IR spectrum of the solid **8**, the S—H stretching vibration of DHLA appears at 2530 cm^{-1}, shifted to lower frequencies relative to that of pure DHLA at 2561 cm^{-1}

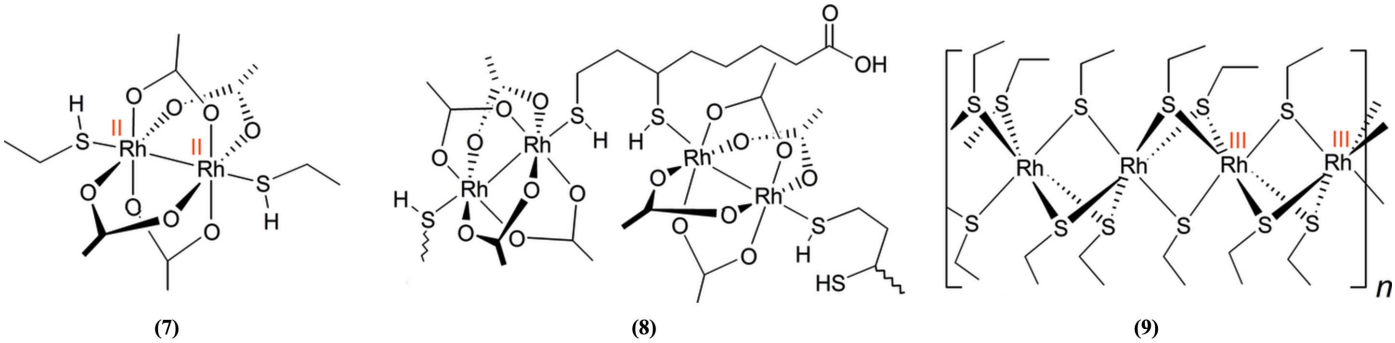

Figure 7
Proposed structures for $[Rh^{II}_2(AcO)_4(EtSH)_2]$ (**7**), $[Rh^{II}_2(AcO)_4(DHLA)]_n$ (**8**), and the reaction product (**9**) of $Rh_2(AcO)_4$ with excess NaEtS under aerobic conditions.

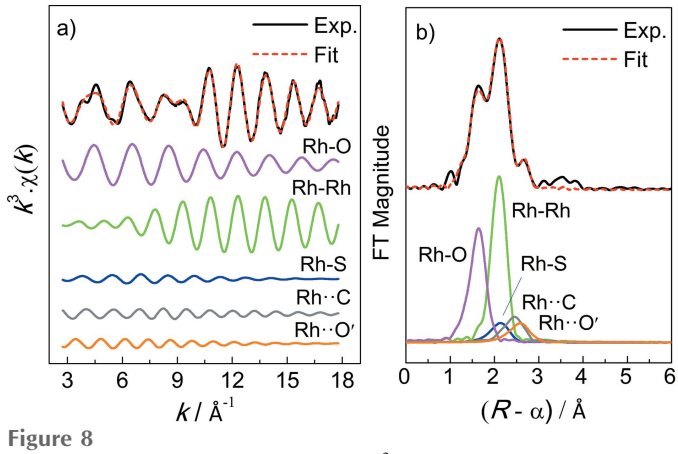

Figure 8
(*a*) Least-squares curve fitting of the k^3-weighted Rh *K*-edge EXAFS spectrum of the $[Rh_2(AcO)_4(DHLA)]_n$ solid (**8**) with separate contributions from the Rh—O, Rh—Rh, Rh—S, Rh···C and Rh···O'_{eq} scattering paths; (*b*) the corresponding Fourier transforms.

(Fig. S6; literature values 2547–2557 cm^{-1}) (Nikolić *et al.*, 2014; Zhang *et al.*, 2013), suggesting that the S—H bond becomes weaker upon coordination of DHLA to the axial positions of $Rh_2(AcO)_4$. Also the S—H stretching frequency for benzylthiol coordinated in $[Rh_2(AcO)_4(HSCH_2Ph)_2]$ (2550 cm^{-1}) shows a similar shift relative to that of pure benzylthiol (2565 cm^{-1}) (Christoph & Tolbert, 1980; Rajalingam *et al.*, 2010). It is unlikely that the DHLA carboxyl group is involved in any bonding interaction in this compound, *e.g.* replacing an acetate group in the $Rh_2(AcO)_4$ cage of **8**, since its 1:1 $Rh_2(AcO)_4$:DHLA composition from elemental analysis confirms that the number of AcO^- ligands remains unchanged. Moreover, the C═O stretching vibrational frequency of the COOH group in **8** (1708 cm^{-1}) is very similar to that in pure DHLA (1707 cm^{-1}), and the $\nu_{asym}(AcO^-)$ vibrational band shifts slightly to a higher frequency (1587 cm^{-1}), relative to that of $Rh_2(AcO)_4$ [1579 cm^{-1}; reported at 1586 cm^{-1} at 80 K (Clark & Hempleman, 1988)]; see Figs. S6 and S7*a*.

The above results show that DHLA in $[Rh_2(AcO)_4(DHLA)]_n$ (**8**) behaves like ethanethiol in $[Rh_2(AcO)_4(EtSH)_2]$ (**7**). Each thiol group of DHLA coordinates via its S atom to the axial position of a $Rh_2(AcO)_4$ unit, thus forming a bridge rather than an (*S,S*)-chelate; *i.e.* it does not behave like the (*S,N*)-donor ligand cysteine, which replaces the acetate groups. The proposed oligomeric structure in Fig. 7 (middle) is deduced from the 1:1 ratio of $Rh_2(AcO)_4$:DHLA in **8**, which is insoluble in all common solvents.

3.3.3. Reactions of $Rh_2(AcO)_4$ with sodium ethanethiolate (NaEtS) and $Na_3(DTLA)$, the sodium dithiolate salt of DHLA. Ethanethiol and DHLA are both weak acids in water (pK_a = 10.6 and 10.7, respectively) (Bhattacharyya & Rohrer, 2012; Fuchs, 1997); however, since their reactions with $Rh_2(AcO)_4$ were not carried out in aqueous media, formation of their conjugate bases was not promoted. Therefore, we reacted their sodium thiolate salts NaEtS and $Na_3(DTLA)$ with $Rh_2(AcO)_4$ in mole ratio 10:1 under aerobic conditions, which produced the precipitates **9** and **10**, respectively. These products were found to be diamagnetic based on magnetic susceptibility measurements and insoluble in common solvents, and therefore considered to be oligomeric (or polymeric) in nature. The empirical formula $[Na_3Rh_7(CH_3CH_2S)_{17}(CH_3COO)_7 0.4H_2O]_n$ is closest to the elemental analysis of **9** (see Section 2.1.4). The presence of bridging acetate groups in compound **9** was confirmed by assigning a band at 1541 cm^{-1} in its IR spectrum to COO^- stretching (see Fig. S7*c*).

The EXAFS oscillations and the corresponding FTs for **9** and **10** were quite different from those of the thiol (EtSH and DHLA) reaction products $[Rh_2(AcO)_4(EtSH)_2]$ (**7**) and $[Rh_2(AcO)_4(DHLA)]_n$ (**8**); see Fig. 5. The XANES spectra of **7** and **9** also display a drastic change in the electronic environment around the Rh ions in these compounds (see Fig. 6). Analyses of the EXAFS data using the *FEFF* files from the optimized geometry for $[Rh_4(EtS)_{15}]^{3-}$, which allowed fitting the FT feature at $(R - \alpha) \simeq 4$ Å, revealed six Rh—S and about two $Rh^{III}\cdots Rh^{III}$ interactions with mean distances of 2.37 ± 0.02 Å and 3.18 ± 0.02 Å, respectively, around each Rh ion in **9** and **10** (see Table 1); the separate contributions from each scattering path to the EXAFS spectrum of the solid **10** are shown in Fig. 9. These distances are close to the average Rh—S and Rh···Rh distances, $Rh-S_{ave}$ = 2.365 Å and $Rh^{III}\cdots Rh^{III}$ = 3.208 Å, in the crystal structure of rhodium(III) sulfide (Rh_2S_3), which comprises of distorted $[ReS_6]$ octahedra and $[SRh_4]$ tetrahedra (Parthé *et al.*, 1967; Tan & Harris, 1998). Also, in the $[Cp^*Rh(\mu\text{-}SPh)_3Rh(\mu\text{-}SPh)_3RhCp^*]Cl$ crystal (CSD code: RUYROT), the average distances around the central Rh(III) ion surrounded by six bridging thiolate S atoms are $Rh-S_{ave}$ = 2.371 Å and $Rh^{III}\cdots Rh^{III}$ = 3.218 Å (Boudreau *et al.*, 2010). Oxidation of the Rh(II) ions in $Rh_2(AcO)_4$ (**1**) to Rh(III) ions in the rhodium-thiolate products **9** and **10** probably occurs in a similar way as the reaction between **1** and glutathione, cysteine and its derivatives, where O_2 is reduced to peroxides (O_2^{2-}) (Jalilehvand *et al.*, 2017; Enriquez Garcia & Jalilehvand, 2018).

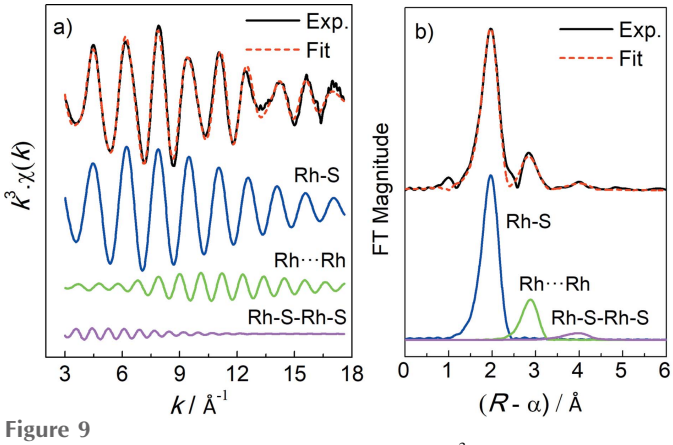

Figure 9
(*a*) Least-squares model curve fitting to the k^3-weighted Rh *K*-edge EXAFS spectrum of solid **10**, *i.e.* the reaction product of $Rh_2(AcO)_4$ with excess $Na_3(DTLA)$; the contributions from the Rh—S, Rh···Rh and Rh—S—Rh—S (n_{leg} = 4; along the linear S—Rh—S entities) scattering paths are shown separately; (*b*) the corresponding Fourier transforms.

The EXAFS spectrum of **9** was also fitted, using the *FEFF* files from the ΔΛ-[Rh{Ir(aet)$_3$}$_2$]Br$_3$ structure, to simulated EXAFS oscillations that also included an Rh—O scattering path because of the presence of acetate groups shown by its FT-IR spectrum (Models **II**–**IV** in Table S2). Assuming an RhS5O coordination (Model **II**) resulted in reasonable distances and σ^2 values; however, the fitting residual increased relative to that of RhS6 coordination (Model **I**); see Fig. S8. Refinement of coordination numbers for all scattering paths (Rh—O, Rh—S and Rh···Rh) led to rejection of the Rh—O path. Fig. 7 (right) displays our proposed structure for compound **9**, while coordination of CH_3COO^- to Rh(III) ions cannot be ruled out.

The XANES features of the oligomeric Rh^{III}–GSH product, $\{Na_2[Rh^{III}_2(HA)_4]\cdot 7H_2O\}_n$ (**2**), resemble those of the reaction product of **1** with excess sodium ethanethiolate (NaEtS) (**9**); see Fig. 6. The FT of the k^3-weighted EXAFS spectrum of **2** shows a small peak at ∼2.8 Å (not corrected for phase shift), as also for compounds **9** and **10**; see Fig. 5 (right). Thus, the model compounds **9** and **10** support our previously proposed structure for the Rh^{III}–GSH product (**2**), in which three glutathione thiolato groups bridge two Rh(III) ions in each dimeric unit, with the Rh···Rh distance refined to 3.11 ± 0.02 Å (see Table 1) (Enriquez Garcia & Jalilehvand, 2018). The main difference is that each Rh(III) ion is surrounded by four thiolates and two O atoms (from $-COO^-$ or H_2O) in **2**, but six thiolates in **9** and **10**.

3.4. XANES simulation

Fig. 10 shows experimental XANES spectra for $[Rh_2(AcO)_4(EtSH)_2]$ (**7**, left) and for the reaction product of $Rh_2(AcO)_4$ with excess NaEtS (**9**, right), compared with XANES spectra simulated for DFT optimized geometries of $[Rh_2(AcO)_4(EtSH)_2]$ and $[Rh_4(EtS)_{15}]^{3-}$, respectively, by means of the *FEFF8.10* program (Ankudinov *et al.*, 1998). The absorption features in the experimental XANES spectra are well reproduced in the simulated XANES spectra, indicating that $[Rh_4(EtS)_{15}]^{3-}$, which is similar to the proposed structure in Fig. 7 (right), is a good structural model for **9**. However, both simulated spectra show an energy shift of about +20 eV relative to the *K*-edge absorption edge. Attempts to reduce the shift using the so-called correction card were unsuccessful. Similar energy shifts of simulated versus experimental XANES spectra have been previously reported (Bosman & Thieme, 2009), and explained based on the inaccuracy in the potentials and the photoelectron self-energy (Rehr & Albers, 2000; Gilbert *et al.*, 2003).

4. Conclusions

The current study shows that monothiol or dithiol ligands with —SH as their only functional group coordinate to the axial positions of $Rh_2(AcO)_4$, keeping the Rh_2^{4+} cage intact (Rh^{II}—Rh^{II} = 2.41 ± 0.02 Å). The energy levels of the $\sigma(Rh_2^{4+})$ and $\pi(Rh_2^{4+})$ orbitals increase, while $\sigma^*(Rh_2^{4+})$ decreases relative to the corresponding orbitals of the aqua complex $[Rh_2(AcO)_4(H_2O)_2]$, shifting the corresponding absorption bands due to $\sigma(Rh_2^{4+})$, $\pi(Rh_2^{4+}) \rightarrow \sigma^*(Rh_2^{4+})$ and $\pi^*(Rh_2^{4+}) \rightarrow \sigma^*(Rh_2^{4+})$ transitions in the UV and visible regions.

In contrast, ligands with thiolate as their only coordination site facilitate the oxidation of $Rh_2(AcO)_4$ under aerobic conditions and break up its cage structure, forming stable oligomeric Rh(III) d^6 low-spin species with three bridging thiolate groups between the Rh(III) ions, each with a RhS_6 coordination environment ($Rh^{III}\cdots Rh^{III} \simeq 3.18 \pm 0.02$ Å).

Even though the current study was carried out in non-aqueous media, the present results may serve as general schemes for 'aerobic' reactions of dirhodium(II) tetracarboxylates with thiol and thiolate ligands. These structural models are consistent with our proposed structure for the aerobic reaction product of $Rh_2(AcO)_4$ with glutathione at physiological pH, $\{Na_2[Rh^{III}_2(HA)_4]\cdot 7H_2O\}_n$, with three bridging thiolates between the Rh(III) ions in dimeric units

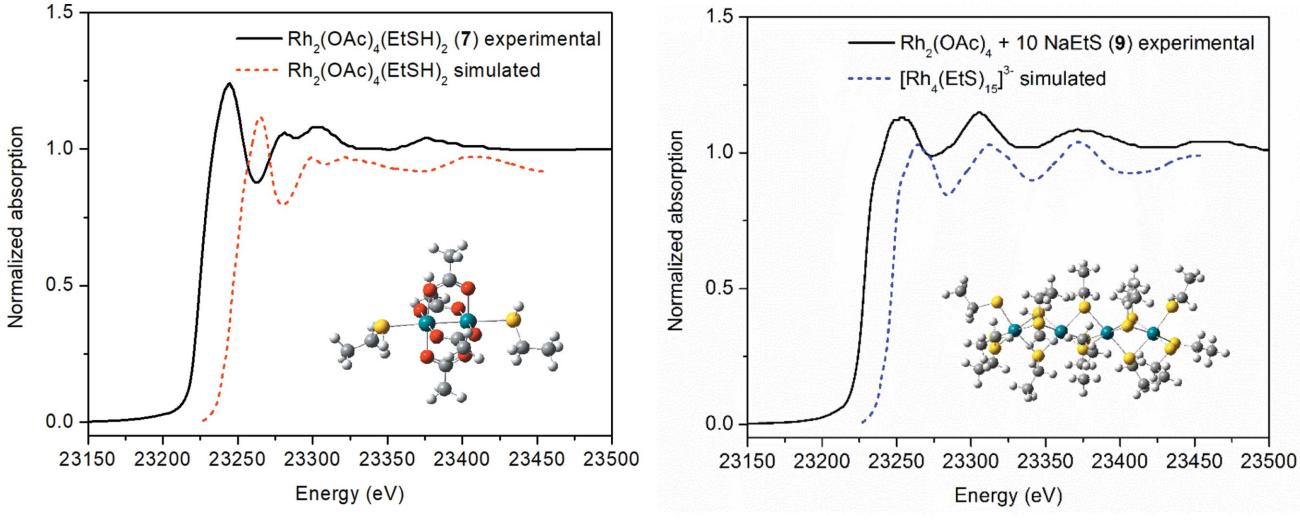

Figure 10
Normalized Rh *K*-edge XANES spectra of $[Rh_2(AcO)_4(EtSH)_2]$ (**7**, left), and the reaction product of $Rh_2(AcO)_4$ with excess NaEtS (**9**, right), compared with the simulated spectra for $[Rh_2(AcO)_4(EtSH)_2]$ and $[Rh_4(EtS)_{15}]^{3-}$ which were shifted down by −0.05 absorption units for clarity.

(Enriquez Garcia & Jalilehvand, 2018). The present results are also applicable for interactions of dirhodium(II) carboxylates with metallothioneins (MTs), the thiol-rich proteins. We propose that under aerobic and physiological conditions the reaction product of $Rh_2(AcO)_4$ with β-MT has a similar structure as the Rh^{III}–GSH compound (**2** in Fig. 1), or a dimeric unit of the model compound **9** (Fig. 7, right), with three β-MT cysteinyl thiolates bridging between the two Rh(III) ions.

Acknowledgements

We are grateful to Professor Arvi Rauk for helpful discussions regarding the theoretical calculations results. AEG acknowledges University of Calgary Eyes High, and Faculty of Science Dean's Open Competitions Doctoral Scholarships. This work was financially supported by the Natural Sciences and Engineering Research Council of Canada (NSERC), Canadian Foundation for Innovation (CFI), the Province of Alberta (Department of Innovation and Science) and the University of Calgary (URGC SEED Grant). Theoretical calculations were performed using the computer resources provided by WestGrid (http://www.westgrid.ca) and Compute/Calcul. Canada (http://www.computecanada.ca). X-ray absorption data collection was carried out at the Stanford Synchrotron Radiation Lightsource (SSRL; Proposal No. 3637). Use of the SSRL, SLAC National Accelerator Laboratory, is supported by the US Department of Energy, Office of Science, Office of Basic Energy Sciences under Contract No. DE-AC02-76SF00515. The SSRL Structural Molecular Biology Program is supported by the DOE Office of Biological and Environmental Research, and by the National Institutes of Health, National Institute of General Medical Sciences (including P41GM103393). The contents of this publication are solely the responsibility of the authors and do not necessarily represent the official views of NSERC, NIGMS or NIH.

Funding information

The following funding is acknowledged: Canada Foundation for Innovation (grant No. 9479 to FJ); Department of Innovation and Science of Province of Alberta (grant to FJ); National Institutes of Health (NIH) – National Institute of General Medical Sciences (grant No. P41 GM103393 to Keith O. Hodgson); Natural Sciences and Engineering Research Council of Canada (grant No. RGPIN-2008-250406 to FJ; grant No. RGPIN-2016-04546 to FJ); University Research Grant Committee, University of Calgary (grant No. SEED Grant 1031019479 to FJ).

References

Aguirre, J. D., Lutterman, D. A., Angeles-Boza, A. M., Dunbar, K. R. & Turro, C. (2007). *Inorg. Chem.* **46**, 7494–7502.
Ankudinov, A. L., Ravel, B., Rehr, J. J. & Conradson, S. D. (1998). *Phys. Rev. B*, **58**, 7565–7576.
Ankudinov, A. L. & Rehr, J. J. (1997). *Phys. Rev. B*, **56**, R1712–R1716.
Bear, J. L., Gray, H. B. Jr, Rainen, L., Chang, I. M., Howard, R., Serio, G. & Kimball, A. P. (1975). *Cancer Chemother. Rep.* **59**, 611–620.
Bear, J. L., Howard, R. A. & Korn, J. E. (1979). *Inorg. Chim. Acta*, **32**, 123–126.
Bhattacharyya, L. & Rohrer, J. S. (2012). Editors. *Applications of Ion Chromatography for Pharmaceutical and Biological Products (Appendix 1)*, pp. 451–453. New York: John Wiley & Sons, Inc.
Bosman, E. & Thieme, J. (2009). *J. Phys. Conf. Ser.* **186**, 012004.
Boudreau, J., Grenier-Desbiens, J. & Fontaine, F.-G. (2010). *Eur. J. Inorg. Chem.* **2010**, 2158–2164.
Boyar, E. B. & Robinson, S. D. (1983). *Coord. Chem. Rev.* **50**, 109–208.
Chen, J. & Kostic, N. M. (1988). *Inorg. Chem.* **27**, 2682–2687.
Chifotides, H. T. & Dunbar, K. R. (2005). *Rhodium Compounds, Multiple Bonds Between Metal Atoms*, edited by F. A. Cotton, C. A. Murillo & R. A. Walton. New York: Springer Science and Business Media Inc.
Chifotides, H. T., Koomen, J. M., Kang, M. J., Tichy, S. E., Dunbar, K. R. & Russell, D. H. (2004). *Inorg. Chem.* **43**, 6177–6187.
Christoph, G. G. & Koh, Y. B. (1979). *J. Am. Chem. Soc.* **101**, 1422–1434.
Christoph, G. G. & Tolbert, M. (1980). *Am. Crystallogr. Assoc. Ser. 2*, **7**, 39.
Clark, R. J. H. & Hempleman, A. J. (1988). *Croat. Chem. Acta*, **61**, 313–329.
Clark, R. J. H., Hempleman, A. J., Dawes, H. M., Hursthouse, M. B. & Flint, C. D. (1985). *J. Chem. Soc. Dalton Trans.* pp. 1775–1780.
Cotton, F. A., DeBoer, B. G., LaPrade, M. D., Pipal, J. R. & Ucko, D. A. (1971). *Acta Cryst.* B**27**, 1664–1671.
Deubel, D. V. & Chifotides, H. T. (2007). *Chem. Commun.* pp. 3438–3440.
Dubicki, L. & Martin, R. L. (1970). *Inorg. Chem.* **9**, 673–675.
Dunbar, K. R., Matonic, J. H., Saharan, V. P., Crawford, C. A. & Christou, G. (1994). *J. Am. Chem. Soc.* **116**, 2201–2202.
Enriquez Garcia, A. & Jalilehvand, F. (2018). *J. Biol. Inorg. Chem.* **23**, 231–239.
Enriquez Garcia, A., Jalilehvand, F., Niksirat, P. & Gelfand, B. S. (2018). *Inorg. Chem.* **57**, 12787–12799.
Erck, A., Rainen, L., Whileyman, J., Chang, I.-M., Kimball, A. P. & Bear, J. (1974). *Proc. Soc. Exp. Biol. Med.* **145**, 1278–1283.
Erck, A., Sherwood, E., Bear, J. L. & Kimball, A. P. (1976). *Cancer Res.* **36**, 2204–2209.
Felthouse, T. R. (1982). *Prog. Inorg. Chem., 29*, 73–166.
Frisch, M. J., Trucks, G. W., Schlegel, H. B., Scuseria, G. E., Robb, M. A., Cheeseman, J. R., Scalmani, G., Barone, V., Petersson, G. A., Nakatsuji, H., Li, X., Caricato, M., Marenich, A., Bloino, J., Janesko, B. G., Gomperts, R., Mennucci, B., Hratchian, H. P., Ortiz, J. V., Izmaylov, A. F., Sonnenberg, J. L., Williams-Young, D., Ding, F., Lipparini, F., Egidi, F., Goings, J., Peng, B., Petrone, A., Henderson, T., Ranasinghe, D., Zakrzewski, V. G., Gao, J., Rega, N., Zheng, G., Liang, W., Hada, M., Ehara, M., Toyota, K., Fukuda, R., Hasegawa, J., Ishida, M., Nakajima, T., Honda, Y., Kitao, O., Nakai, H., Vreven, T., Throssell, K., Montgomery, J. A., Peralta, J. J. E., Ogliaro, F., Bearpark, M., Heyd, J. J., Brothers, E., Kudin, K. N., Staroverov, V. N., Keith, T., Kobayashi, R., Normand, J., Raghavachari, K., Rendell, A., Burant, J. C., Iyengar, S. S., Tomasi, J., Cossi, M., Millam, J. M., Klene, M., Adamo, C., Cammi, R., Ochterski, J. W., Martin, R. L., Morokuma, K., Farkas, O., Foresman, J. B. & Fox, D. J. (2016). *Gaussian 16*, Revision B.01. Gaussian, Inc., Wallingford, CT, USA.
Fuchs, J. (1997). *Lipoic Acid in Health and Disease.* New York: CRC Press.
García, C. F., McKervey, M. A. & Ye, T. (1996). *Chem. Commun.* pp. 1465–1466.
Gilbert, B., Frazer, B. H., Belz, A., Conrad, P. G., Nealson, K. H., Haskel, D., Lang, J. C., Srajer, G. & De Stasio, G. (2003). *J. Phys. Chem. A*, **107**, 2839–2847.

Hansen, J. & Davies, H. M. L. (2008). *Coord. Chem. Rev.* **252**, 545–555.
Howard, R. A., Spring, T. G. & Bear, J. L. (1976). *Cancer Res.* **36**, 4402–4405.
Howard, R. A., Spring, T. G. & Bear, J. L. (1977). *J. Clin. Hematol. Oncol.* **7**, 391–400.
Ioannou, P. V. & Tsivgoulis, G. M. (2014). *Monatsh. Chem.* **145**, 897–909.
Jakimowicz, P., Ostropolska, L. & Pruchnik, F. P. (2000). *Met.-Based Drugs*, **7**, 201–209.
Jalilehvand, F., Enriquez Garcia, A. & Niksirat, P. (2017). *Am. Chem. Soc. Omega*, **2**, 6174–6186.
Johnson, S. A., Hunt, H. R. & Neumann, H. M. (1963). *Inorg. Chem.* **2**, 960–962.
Kitchens, J. & Bear, J. L. (1969). *J. Inorg. Nucl. Chem.* **31**, 2415–2421.
Kraatz, H. B., Jacobsen, H., Ziegler, T. & Boorman, P. M. (1993). *Organometallics*, **12**, 76–80.
Kubicki, M. M., Oudet, P., Martin, C. & Barré, C. (1995). *J. Chem. Soc. Dalton Trans.* pp. 3699–3704.
Mahboob, N., Miyashita, Y., Yamada, Y., Fujisawa, K. & Okamoto, K. (2004). *Inorg. Chim. Acta*, **357**, 75–82.
Miller, D. J. & Moody, C. J. (1995). *Tetrahedron*, **51**, 10811–10843.
Nikolić, R. S., Krstić, N. S., Nikolić, G. M., Kocić, G. M., Cakić, M. D. & Anđelković, D. H. (2014). *Polyhedron*, **80**, 223–227.
Norman, J. G. & Kolari, H. J. (1978). *J. Am. Chem. Soc.* **100**, 791–799.
Norman, J. G., Renzoni, G. E. & Case, D. A. (1979). *J. Am. Chem. Soc.* **101**, 5256–5267.
Orpen, A. G. & Connelly, N. G. (1990). *Organometallics*, **9**, 1206–1210.
Parthé, E., Hohnke, E. & Hulliger, F. (1967). *Acta Cryst.* **23**, 832–840.
Pneumatikakis, G. & Psaroulis, P. (1980). *Inorg. Chim. Acta*, **46**, 97–100.
Rajalingam, K., Hallmann, L., Strunskus, T., Bashir, A., Wöll, C. & Tuczek, F. (2010). *Phys. Chem. Chem. Phys.* **12**, 4390–4399.
Ravel, B. (2001). *J. Synchrotron Rad.* **8**, 314–316.
Rehr, J. J. & Albers, R. C. (2000). *Rev. Mod. Phys.* **72**, 621–654.
Ressler, T. (1998). *J. Synchrotron Rad.* **5**, 118–122.
Shannon, R. D. (1976). *Acta Cryst.* A**32**, 751–767.
Sorasaenee, K., Galán-Mascarós, J. R. & Dunbar, K. R. (2002). *Inorg. Chem.* **41**, 433–436.
Sorasaenee, K., Galán-Mascarós, J. R. & Dunbar, K. R. (2003). *Inorg. Chem.* **42**, 661–663.
Sowa, T., Kawamura, T., Shida, T. & Yonezawa, T. (1983). *Inorg. Chem.* **22**, 56–61.
Spuches, A. M., Kruszyna, H. G., Rich, A. M. & Wilcox, D. E. (2005). *Inorg. Chem.* **44**, 2964–2972.
Tan, A. & Harris, S. (1998). *Inorg. Chem.* **37**, 2215–2222.
Wilson, C. R. & Taube, H. (1975). *Inorg. Chem.* **14**, 2276–2279.
Wong, D. L. & Stillman, M. J. (2016). *Chem. Commun.* **52**, 5698–5701.
Wong, D. L., Zhang, A., Faponle, A. S., de Visser, S. P. & Stillman, M. J. (2017). *Metallomics*, **9**, 501–516.
Yoshimura, T., Umakoshi, K. & Sasaki, Y. (2003). *Inorg. Chem.* **42**, 7106–7115.
Zabinsky, S. I., Rehr, J. J., Ankudinov, A., Albers, R. C. & Eller, M. J. (1995). *Phys. Rev. B*, **52**, 2995–3009.
Zhang, C., Sun, X., Li, J. & Liu, Y.-N. (2013). *Nanoscale*, **5**, 6261–6264.
Zhang, X., Ma, M. & Wang, J. (2003). *ARKIVOC*, **(ii)**, 84–91.